PHYSICAL REVIEW FLUIDS **2**, 044201 (2017)

Inertial migration regimes of spherical particles suspended in square tube flows

Hiroyuki Shichi and Hiroshi Yamashita
Graduate School of Engineering and Science, Kansai University, Osaka 564-8680, Japan

Junji Seki, Tomoaki Itano, and Masako Sugihara-Seki
Department of Pure and Applied Physics, Kansai University, Osaka 564-8680, Japan

(Received 14 November 2016; published 12 April 2017)

The inertial migration of neutrally buoyant spherical particles suspended in tube flows of square cross sections was investigated experimentally in the range of Reynolds numbers (Re) from 1 to 800 for particle-to-tube-size ratios from 0.075 to 0.175. Direct observations of the particle distribution in the cross section at various distances from the tube inlet revealed that at low Re, smaller than a certain critical value, particles were focused on four equilibrium positions, located at the center of channel faces, consistent with previous studies on microchannel flows, whereas at higher Re, larger than another critical value, four additional equilibrium positions were observed near the channel corners. At intermediate Re, between these two critical values, we observed new focusing positions of particles, located on a heteroclinic orbit joining the channel face and corner equilibrium positions. Comparing these results with corresponding numerical simulations, we examined the migration properties in detail and categorized their types. It was found that the critical Re values depended considerably on the particle-to-tube-size ratio.

DOI: 10.1103/PhysRevFluids.2.044201

I. INTRODUCTION

More than 50 years ago, Segre and Silberberg [1,2] first reported that neutrally buoyant spherical particles suspended in circular tube flows migrated laterally to an equilibrium radial position, approximately 0.6 times the tube radius from the axis, at low Reynolds numbers (Re). This phenomenon, referred to as the Segre-Silberberg effect, is due to the effect of inertia because the reversibility of the Stokes equations prohibits movement of a rigid spherical particle across streamlines in circular tube flows [3].

Recently, inertial migration phenomena of suspended particles flowing through microchannels [4–6] have gained considerable attention in the field of microfluidics due to their broad range of applications, such as in the separation and filtration of particles and biological cells [7–10]. In microfluidics, channels of rectangular cross sections, rather than circular cross sections, are commonly used. For Re below about 100, experimental studies using square microchannels have shown the presence of four equilibrium positions for spherical particles, centered at the faces of the channel [4,11,12]. For higher Re, microchannel experiments using rectangular cross sections, of aspect ratio 1.6, indicated complex variations in equilibrium positions, located at the center of the channel faces, with Re up to 1500 [13].

Although the lateral migration of rigid spherical particles suspended in rectangular channel flows has been studied extensively from various aspects, including numerical and theoretical analyses [14–20], details of the migration properties remain unclear at higher Re (>100). Considering the potential for high-throughput particle separation and analysis, understanding these migration properties could provide a fundamental basis for rational designs of inertial microfluidic systems [13].

Quite recently, macroscale experiments using square tubes of widths of several millimeters, performed in our laboratory in the range of Re from 100 to 1200, confirmed the presence of four equilibrium positions, centered at the faces of the tube at low Re [21], in accordance with microscale experiments [4,11,12,17]. At higher Re, unique patterns of the particle distribution were observed over the square cross section, indicating the emergence of new equilibrium positions, located near the corners of the cross section [21]. These new equilibrium positions were named the *channel corner equilibrium position* (CCE), and the equilibrium positions located at the center of channel faces were named the *channel face equilibrium position* (CFE) [21].

Although the coexistence of the CFE and CCE at high Re (>500) did not match the previous numerical results of Chun and Ladd [22] for a comparable size ratio of the particle diameter to the tube width ($=0.11$), this finding was supported by the numerical simulation of Nakagawa *et al.* [23]. This numerical simulation [23] revealed that the CCE was present even at low Re, but it was unstable for Re below a critical Re. The presence of an unstable equilibrium position near the channel corner at low Re was also demonstrated theoretically [19] and numerically [17]. Furthermore, it was predicted that in a limited range of Re near the critical Re, another type of equilibrium position appears on a heteroclinic orbit joining the CFE and CCE in the cross section [23]. This range of Re was from about 250 to 500 for a size ratio of the particle diameter to the channel width of ~ 0.11.

In the present study, we observed these three types of equilibrium positions directly using submillimeter-sized square tubes, with an emphasis on their variation with Re and their evolution with the axial distance from the tube inlet. The use of tubes of small widths allows us to observe the particle distribution at much more distant cross sections relative to the tube width than the experiments using macroscale tubes. Here, we term the new equilibrium position appearing on a heteroclinic orbit the *intermediate equilibrium position* (IME) and investigate the transition of these equilibrium positions.

Most existing experimental studies observing the particle distribution over the microchannel cross section were performed in the transverse direction, perpendicular to the channel axis, as in typical microscopic observations. In this transverse observation, it is generally hard to detect accurately the height of particles from the channel bottom, except in several three-dimensional observation methods, such as the digital holographic technique [12,24] and laser scanning confocal microscopy [4].

In the present study, we have applied the *en face* observation method, used for macroscale tube flows [21], to submillimeter-sized tube flows, in which the cross section of the tube at a small distance upstream of the outlet was observed longitudinally from the downstream side along the center axis of the tube using a long-working-distance objective and a high-speed camera. This method enabled us to detect directly the position of each particle flowing across the cross section of the tube with high spatial resolution.

Using this method, we observed the distribution of neutrally buoyant spherical particles over the square cross section of width $D = 400$–$800\ \mu\text{m}$ for $\text{Re} = 1$–800. The use of tubes with various lengths ($L = 20$–600 mm) revealed the evolution of the distribution of particles along the flow, focusing on equilibrium positions in downstream cross sections. Comparing the results obtained with corresponding numerical simulations, we examined the migration property of particles in square tube flows, depending on Re, and categorized their types for the particle-to-tube-size ratio $d/D = 0.075$–0.175.

II. MATERIAL AND METHODS

Polystyrene spherical particles (Thermo Scientific, USA) with a mean diameter $d = 30$–$70\ \mu\text{m}$ were suspended in glycerol-water solution at volume fractions of $(1.3$–$3.6 \times 10^{-2})\%$ such that particle-particle interactions were minimized. The density of the fluid was matched carefully to that of the particles, $\rho = 1.052$–$1.054 \times 10^{3}\ \text{kg m}^{-3}$, and its viscosity was $\eta = 1.65$–1.87×10^{-3} Pa s.

The experimental setup is shown in Fig. 1. A borosilicate square capillary (VitroCom, USA) of width $D = 400$–$800\ \mu\text{m}$ and length $L = 20$–600 mm was immersed in the glycerol-water solution bath, and the particle suspension was flowed through the tube at controlled rates using a syringe pump (Harvard 11 Elite, USA). The tube cross section about 2–3 mm upstream of the outlet was illuminated with a laser light sheet produced with a 100-mW optically pumped semiconductor laser (OPSL, Coherent OBIS640, USA, 640 nm). The cross section of the tube was imaged from the

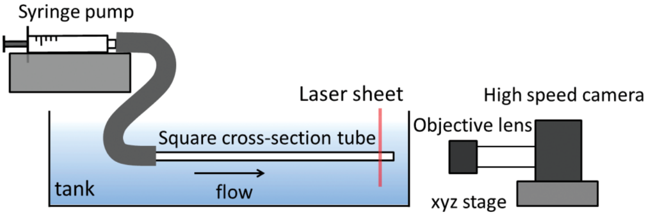

FIG. 1. Experimental setup.

downstream side along the center axis of the tube using a high-speed camera (Photron FASTCAM mini UX50, AX100, Japan) equipped with a long-working-distance objective (Edmund Optics PlanAPO 10×, 20×, USA) at a frame rate of 100–10,000 frames/s.

The images obtained were analyzed with the public-domain software IMAGEJ (National Institutes of Health, USA) to yield the positions of the particle center in the cross section. The pixel size was typically $\sim 1 \times 1\ \mu\text{m}^2$. In each experiment, the positions of more than 250 particles were detected.

The Reynolds number was defined as $\mathrm{Re} = \rho U D/\eta$, where U is the average flow velocity. The particle-scale Reynolds number can be defined as $\mathrm{Re}_\mathrm{p} = \mathrm{Re}(d/D)^2$. In the present study, we assessed cases of size ratio $d/D = 0.075$–0.175 and $\mathrm{Re} = 1$–800, corresponding to $\mathrm{Re}_\mathrm{p} = 0.006$–$24.5$. The ratio of the tube length to the tube width L/D ranged from 50 to 1500.

In Sec. III A, we show some numerical results for comparison with the present experimental results. The numerical results of the particle trajectories for size ratio $d/D = 0.125$ were reported recently in Yamashita and Sugihara-Seki [25]. The computational method was presented previously [23]. Briefly, we analyzed the trajectories of a neutrally buoyant rigid spherical particle immersed in a pressure-driven flow through a square tube using the immersed boundary method proposed by Kajishima *et al.* [26]. The size of the spatial mesh ($0.05d$) and the axial length of the computational domain ($20d$) were the same as in Ref. [23]; they were determined based on an accuracy assessment of the numerical computation as described in Ref. [23]. The numerical error of the force exerted on the particle was estimated to be at most 5%.

III. RESULTS AND DISCUSSION

A. Three types of equilibrium positions

As representative examples of the present experimental results, Figs. 2(a)–2(e), 2(f)–2(j), and 2(k)–2(o) illustrate the evolution of the particle distribution in the flow direction for $d/D = 0.125$ at $\mathrm{Re} = 100$, 280, and 450, respectively. Each dot in these figures represents the position of the particle center. The particle distribution of larger L/D corresponds to that of a cross section located farther downstream from the tube inlet. Figures 2(e), 2(j), and 2(o), which represent the particle distribution obtained at the most distant downstream cross section, show clearly the particle focusing on the three types of equilibrium positions mentioned in the Introduction. At $\mathrm{Re} = 100$, particles were focused at the centers of the faces [CFE, Fig. 2(e)]; additional focusing points can be seen at intermediate positions, symmetric with respect to the diagonals at $\mathrm{Re} = 280$ [IME, Fig. 2(j)] and on the diagonals near the corners at $\mathrm{Re} = 450$ [CCE, Fig. 2(o)].

In our laboratory, the motion of a spherical particle immersed in square cross-section tube flows was analyzed numerically, using an immersed boundary method [23,25]. To better understand the migration properties in square tube flows, we plotted the numerical results for parameter values corresponding to Fig. 2, i.e., $d/D = 0.125$ and $\mathrm{Re} = 100$, 280, and 450, in Figs. 3(a), 3(e), and 3(i), respectively [25]. In the tube cross section, the y and z axes are taken parallel to the tube walls, with the origin at the center of the cross section. From symmetry considerations, the region of the azimuthal angle θ between zero and $\pi/4$ relative to the y axis was plotted; each line in Figs. 3(a), 3(e),

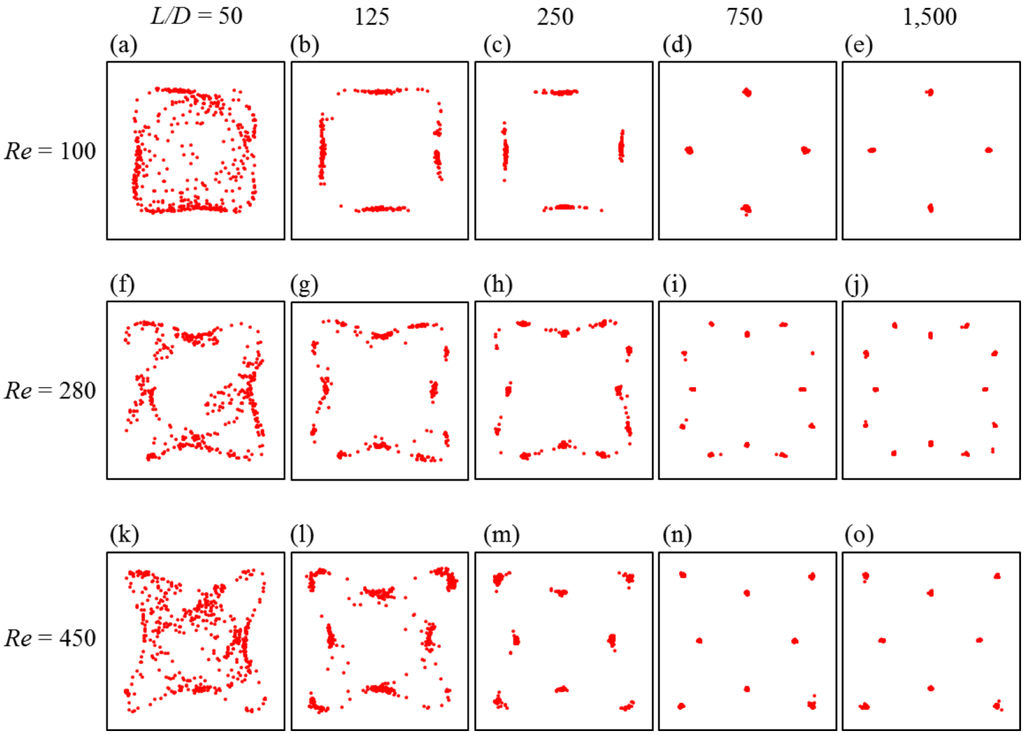

FIG. 2. Particle distributions over the tube cross section for $d/D = 0.125$ at various distances from the tube inlet. (a)–(e) Re = 100, (f)–(j) Re = 280, and (k)–(o) Re = 450.

and 3(i) represents the trajectory of the particle center projected on the cross section (y-z plane), starting at various initial positions marked by crosses.

Comparisons between the present experimental results and numerical results are shown in Figs. 3(b)–3(d), 3(f)–3(h), and 3(j)–3(l) at Re $=$ 100, 280, and 450, respectively. The particle positions over the whole cross section shown in Fig. 2 were summed in the triangular region of $0 \leqslant \theta \leqslant \pi/4$ from symmetry considerations; the particle distribution obtained was plotted in the first quadrant in Figs. 3(b)–3(d), 3(f)–3(h), and 3(j)–3(l) for $L/D = 50$, 125, and 750, together with the numerical results shown in Figs. 3(a), 3(e), and 3(i).

We consider each case of Re $=$ 100, 280, and 450 in detail. Figures 2(a)–2(e) present direct observations of the evolution of the particle focusing towards the CFE at Re $=$ 100. The presence of four equilibrium positions centered at the channel faces at low Re was reported previously from experimental studies using square microchannels [4,11,12,17], numerical simulations using a finite-element method [11] and a force coupling method [17], and theoretical analyses based on the asymptotic expansion method [19].

At Re $=$ 100, the numerical simulation shown in Fig. 3(a) predicted the presence of an equilibrium position, located on the diagonal, near the corner [CCE, square in Fig. 3(a)] in addition to the CFE on the y (or z) axis (circle), where the resulting lateral force exerted on the particle vanishes. In Fig. 3(a), the particle trajectories, starting at various initial positions in the cross section except on the diagonal, finally approach the CFE, indicating that the CFE is stable, whereas the CCE is unstable. This result accounts for the experimental observation that the CCE has not been observed at this Re.

Figures 2(a)–2(e) and 3(b)–3(d) indicate that particles entering randomly from the tube inlet migrate first towards a ring that is nearly parallel to the tube wall [Figs. 2(a), 2(b), 3(b), and 3(c)], and then they move along the ring towards the CFE [Figs. 2(c)–2(e) and 3(d)]. This feature is similar to the two-stage migration reported previously from the numerical simulation of Chun and

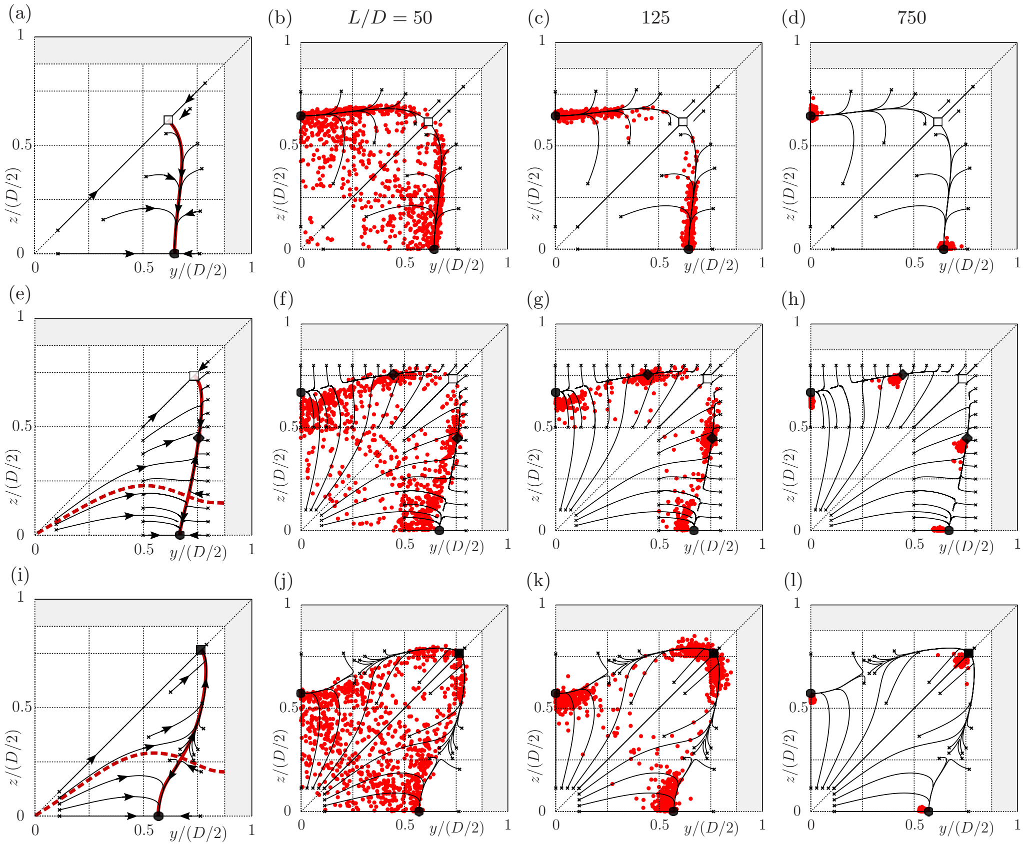

FIG. 3. (a), (e), and (i) Results of the numerical simulation for $d/D = 0.125$ [25], corresponding to Fig. 2: (a) Re = 100, (e) Re = 280, and (i) Re = 450. Solid lines with arrows: particle trajectories starting from the location of crosses; circles: CFE; squares: CCE; diamonds: IME; thick solid red lines: pseudo-Segre-Silberberg ring; thick red dashed lines: separatrix. (b)–(d), (f)–(h), and (j)–(l) Comparisons of the present experimental results shown in Fig. 2 (red dots) and numerical results (solid lines) for $d/D = 0.125$ at Re = 100, 280, and 450, respectively.

Ladd [22], although their particle focusing points are not necessarily in accordance with the present or previous results [4,11,12,17,19,21,23]. As shown in Figs. 3(b)–3(d), the present study showed that the ring corresponds to the heteroclinic orbit [thick red line in Fig. 3(a)] joining the CFE and CCE. For a particle located on the ring, the resultant lateral force perpendicular to the ring vanishes, and the force component along the ring is very small [23,25]. Choi *et al.* [12] termed the ring formed at the end of the first stage the pseudo-Segre-Silberberg annulus after the Segre-Silberberg annulus observed in circular tube flows [2]. In the present paper, we call this ring the *pseudo-Segre-Silberberg ring* (pSS ring). These migration properties at low Re were consistent with previous microscale experiments [12,17] (Re $<$ 120), numerical simulations [17], and theoretical analyses [19].

Figures 2(f)–2(j) and 2(k)–2(o) present the evolutions of the particle distributions along the flow direction at Re = 280 and 450, respectively. These particle distributions have not been found previously in experimental studies using microchannels. However, in macroscale experiments using millimeter-sized tubes, similar patterns of particle distributions have been reported at comparable Re [21]; however, the focusing of almost all particles on the equilibrium positions, as shown in Figs. 2(j) and 2(o), has not been observed before due to limitations of the tube length relative to the tube width, i.e., small L/D, for macrosized tubes.

The numerical simulations shown in Figs. 3(e) and 3(i), together with Figs. 3(f)–3(h) and 3(j)–3(l), predict two important features of these cases, which are also common to the low Re case considered above [Figs. 3(a)–3(d)]. First, both the CFE and CCE are always present, and the former is stable regardless of Re. Second, the pSS ring exists even at high Re, and particles migrate towards stable equilibrium positions in two stages; in the first stage, they move towards the pSS ring (thick solid red line in Fig. 3), and in the second stage they travel along the pSS ring towards either stable equilibrium position, depending on their initial positions. As can be seen more clearly in Sec. III C, an increase in Re beyond 150–200 shifts the CFE towards the tube center, whereas it shifts the CCE towards the tube wall. Following these shifts, the pSS ring is deformed into a ring with a concavity near the centers of the channel faces to a greater extent with increasing Re. This deformation of the pSS ring and the two-stage migration properties are evident, experimentally and numerically (Figs. 2 and 3).

Let us take a closer look at the case in Figs. 2(k)–2(o) at $\mathrm{Re} = 450$ before the case of $\mathrm{Re} = 280$ for ease of understanding. Figure 2(o) shows that, in experiments, particles were focused at eight points in the downstream cross section, four of which were the CFE already seen at low Re, and the others were the CCE, located on the diagonals near the corners. The corresponding numerical simulation, shown in Fig. 3(i), predicts that particles starting at various initial positions migrate in two stages towards either the CFE (circle) or the CCE (square), indicating that both of these types of equilibrium positions are stable. This feature could rationalize the evolution of the particle distribution obtained experimentally [Figs. 2(k)–2(o) and 3(j)–3(l)]. Thus, there is a critical Re at which the CCE exhibits a transition between unstable and stable states. For Re larger than this critical Re, particles would be focused on four points of the CCE as well as four points of the CFE in the tube cross section.

Figure 3(i) indicates that the tube cross section can be divided into two regions, depending on the type of equilibrium positions the particle will finally reach, and these two regions are separated by a separatrix [thick red dashed line in Fig. 3(i)]. The intersection of the separatrix and the pSS ring represents a saddle point.

In Fig. 3(l) [and Fig. 3(h)], we may notice slight discrepancies of locations between numerically obtained equilibrium positions and experimentally obtained particle focusing points. These may result from experimental and numerical errors. One of the causes may be the round corners of the tube cross section shown in Fig. S1(a) in the Supplemental Material [27] since we assumed a square cross section with sharp corners in the numerical simulation.

We next consider the case of Figs. 2(f)–2(j) at $\mathrm{Re} = 280$. Figure 2(j) shows that in experiments, eight new focusing points appeared in addition to the four points of the CFE; these correspond to the IME and are located symmetrically with respect to the diagonals of the cross section. Their azimuthal angle was $\theta_\mathrm{e} \sim 0.51$ rad. These focusing properties of the particles can be predicted from the corresponding numerical simulation, shown in Fig. 3(e), which indicates the emergence of a new equilibrium position (diamond) on the pSS ring, with $\theta_\mathrm{e} \sim 0.54$ rad, comparable to the experimental observation.

Additionally, from the particle trajectories shown in Fig. 3(e), it can be seen that both CFE and IME are stable, which may explain the experimental observation of the particle focusing on these equilibrium positions. As Re increases from a small value, the IME appears at a certain Re, and a further increase in Re increases the azimuthal angle θ_e of the IME up to $\pi/4$ rad [see details in Sec. III C]. The CCE is always present in the Re range examined, whether stable or not, whereas the IME exists in a limited range of Re on the pSS ring. Additionally, the IME may not be a single focusing point; rather, multiple focusing points may appear on the pSS ring at certain Re, as typically seen below in Sec. III B.

From the particle distributions obtained, we determined the location of each equilibrium position as the local maximum of the probability density function, in a manner similar to our previous study for macroscaled tube flows [21]. The locations of the CFE, IME, and CCE thus obtained for the cases shown in Fig. 2 are plotted as a function of $L/D (\geqslant 125)$ in Figs. 4(a)–4(c). The standard deviations of the locations obtained were less than $0.01 \times (D/2)$, except for the IME and CCE at $L/D = 125$. In these two cases, the standard deviations were about $0.03 \times (D/2)$, which may result from the insufficient focusing of particles at a small distance from the tube inlet, rather than the measurement error.

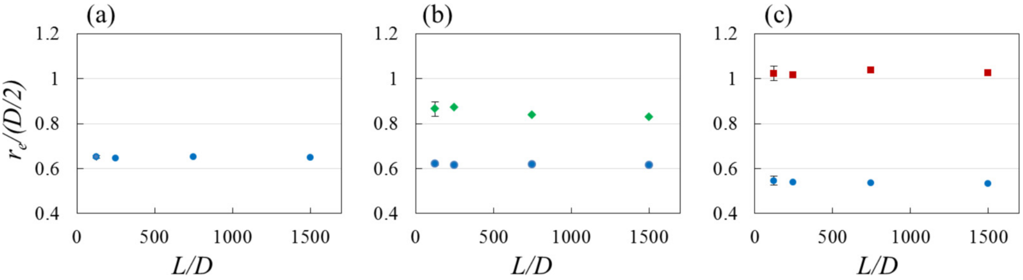

FIG. 4. Radial distances from the tube center of the CFE (circles), IME (diamonds), and CCE (squares), corresponding to Fig. 2, for $d/D = 0.125$ at (a) Re = 100, (b) 280, and (c) 450. The error bar shows the standard deviation at $L/D = 125$. The standard deviations at $L/D \geqslant 250$ are smaller than the symbol size.

Figures 4(a)–4(c) indicate that the locations of the equilibrium positions were almost independent of L/D for $L/D \geqslant 125$. This was also true for the IME, indicating that particles were not placed transiently in that position but that the resulting lateral force exerted on the particles vanishes there.

B. Transition of equilibrium positions

The present experimental results suggest the presence of at least two critical Reynolds numbers, Re_{c1} and Re_{c2}. Here, Re_{c1} represents the Re value at which the IME emerges, and Re_{c2} represents the Re value at which the CCE appears; that is, it shows the transition between unstable and stable states. In terms of Re_{c1} and Re_{c2}, the particle migration properties can possibly be classified into three regimes by Re: $\mathrm{Re} < \mathrm{Re}_{c1}$, $\mathrm{Re}_{c1} < \mathrm{Re} < \mathrm{Re}_{c2}$, and $\mathrm{Re}_{c2} < \mathrm{Re}$, corresponding to Figs. 2(a)–2(e), 2(f)–2(j), and 2(k)–2(o), respectively. In the first regime (regime 1), the particles are focused only on the CFE. In the second and third regimes (regimes 2 and 3), the IME and CCE are added as focusing points, respectively. The values of Re_{c1} and Re_{c2} vary depending on the size ratio d/D but are independent of L/D.

To assess the values of Re_{c1} and Re_{c2}, the variation of the particle distribution with Re was plotted in Fig. 5 for $d/D = 0.125$, $L/D = 750$, and Re = 3–600. For $\mathrm{Re} \leqslant 240$, shown in Figs. 5(a)–5(d), the particle focusing points were only the CFE (regime 1). In the cases in Figs. 5(a) and 5(b), the

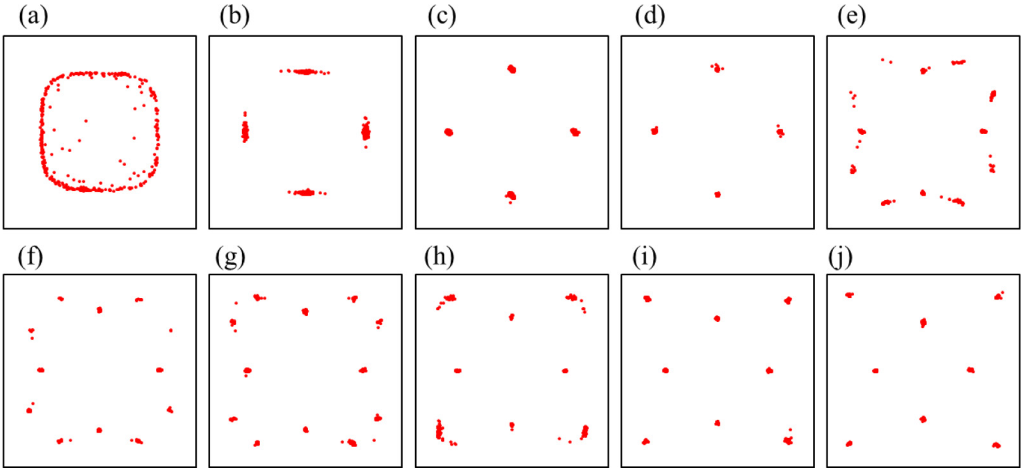

FIG. 5. Particle distributions over the tube cross section for $d/D = 0.125$ and $L/D = 750$ at (a) Re = 3, (b) 30, (c) 100, (d) 240, (e) 260, (f) 280, (g) 300, (h) 400, (i) 450, and (j) 600.

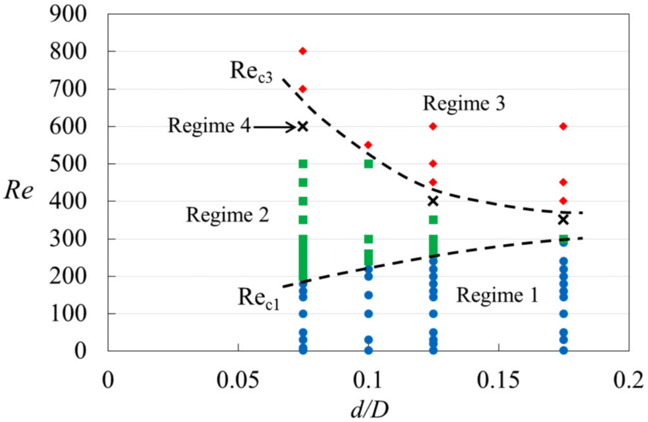

FIG. 6. Regimes of the particle migration (regime 1: circles, regime 2: squares, regime 3: diamonds, and regime 4: crosses). The dashed lines represent approximate values of Re_{c1} and Re_{c3}.

particles were observed to be focused on the CFE at cross sections farther downstream. In Fig. 5(e) at $\mathrm{Re} = 260$, particles were seen at the IME, so Re_{c1} can be estimated to be between 240 and 260. In Figs. 5(e)–5(h) at $\mathrm{Re} = 260$–400, particles were focused at the CFE and the IME (regime 2). However, in Figs. 5(i) and 5(j) at $\mathrm{Re} = 450$ and 600, the IME was absent, and particles were focused on the CCE and CFE (regime 3).

Here, we note that in Fig. 5(h) at $\mathrm{Re} = 400$ ($\sim\mathrm{Re}_{c2}$), several particles are also present on the CCE in addition to the CFE and IME, suggesting their coexistence. If this is the case, Re_{c2} is below 400, and it may be necessary to define another critical Re, Re_{c3}, at which the azimuthal angle of the IME reaches $\pi/4$; that is, the IME merges with the CCE. Thus, a new regime (regime 4) may exist in the range of $\mathrm{Re}_{c2} < \mathrm{Re} < \mathrm{Re}_{c3}$, where the particle focusing points are the CFE, IME, and CCE. In experiments, it is not easy to determine confidently the value of Re_{c2} or the presence of the CCE near that Re because the number of particles located at that position is small at $\mathrm{Re} \sim \mathrm{Re}_{c2}$. In this study, we assumed that the CCE was present if the number of particles observed at that position was larger than 1% of the total number. Based on this criterion, the CCE is present in the case shown in Fig. 5(h) at $\mathrm{Re} = 400$ (regime 4), but it is absent in Fig. 5(g) at $\mathrm{Re} = 300$, where only a few particles were observed near the channel corner (regime 2). These classifications were unchanged for the particle distributions obtained at $\mathrm{Re} = 300$ and 400 for larger L/D ($= 1500$).

In Fig. 6, the regimes of particle migration obtained in the present experiments are summarized for various d/D from 0.075 to 0.175, including regime 4 (crosses in Fig. 6). Experiments using tubes of different lengths also suggested the presence of regime 4 for the parameter values corresponding to the crosses in Fig. 6 (see Fig. S4 in the Supplemental Material [27]). Because regime 4 was observed in limited ranges of Re for each d/D, we concluded that $\mathrm{Re}_{c2} \sim \mathrm{Re}_{c3}$. Figure 6 indicates that an increase in d/D from 0.075 to 0.175 increased Re_{c1}, whereas it decreased Re_{c3} ($\sim\mathrm{Re}_{c2}$).

C. Locations of focusing points

Figure 7 illustrates the variations in the locations of the particle focusing points with Re for size ratios $d/D = 0.075, 0.10, 0.125$, and 0.175. The radial distances r_e from the tube centerline are shown for the CFE in Fig. 7(a) and for the IME and CCE in Fig. 7(b). The azimuthal angles θ_e relative to the y axis are plotted for the IME and CCE in Fig. 7(c). In the inset in Fig. 7(a), previous results of microchannel experiments are also shown for the CFE at $d/D = 0.075$ [12], 0.11 [17], and 0.16 [12] for reference. For the location of the particle focusing points, the measurement errors were estimated to be at most several pixels $\sim O(0.01 \times (D/2))$, as noted for the data in Fig. 4.

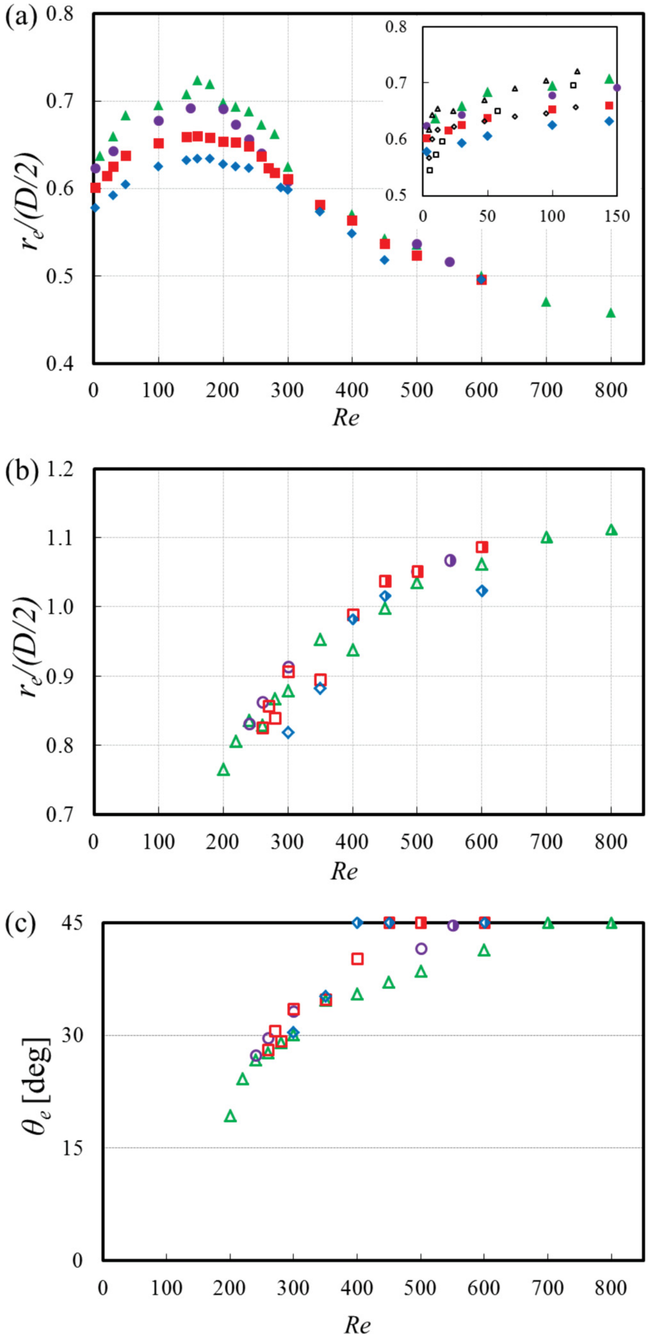

FIG. 7. (a) Radial distances from the tube center of the CFE, (b) radial distances of the IME and CCE, and (c) azimuthal angles of the IME and CCE. Solid, half-solid, and open symbols in different colors represent the CFE, CCE, and IME, respectively, for $d/D = 0.075$ (triangles), 0.10 (circles), 0.125 (squares), and 0.175 (diamonds). In the inset in (a), the results of previous microscale experiments for the CFE are shown by black symbols for $d/D = 0.075$ (triangles) [12], 0.11 (squares) [17], and 0.16 (diamonds) [12].

In Fig. 7(a), the CFE was shifted in the outward direction with increasing Re, followed by an inward shift for Re beyond 150–200. The former outward shift is consistent with the observations of the microscale experiments at low Re [11,12,17]; the latter inward shift agrees with the macroscale experiments for $d/D = 0.11$ [21]. However, the IME and CCE moved monotonically farther from the tube center with increasing Re. This trend is in accordance with the macroscale experimental results at high Re up to Re $= 1{,}200$ [21]. Figure 7(a) also shows that the CFE of larger particles were located closer to the tube center at low Re, which agrees with previous studies for microchannel flows [11,19]. However, the locations of the CFE at relatively high Re and the other equilibrium positions (CCE and IME) were nearly insensitive to the size ratio d/D in the range of $0.075 \leqslant d/D \leqslant 0.175$.

In Fig. 7(c), data with $\theta_{\mathrm{e}} \sim \pi/4$ represent the CCE, while data with $0 < \theta_{\mathrm{e}} < \pi/4$ in the Re range between $\mathrm{Re}_{\mathrm{c1}}$ and $\mathrm{Re}_{\mathrm{c3}}$ represent the IME. The azimuthal angles of the CFE were nearly zero (data not shown). Figure 7(c) indicates that, as Re increases beyond $\mathrm{Re}_{\mathrm{c1}}$ up to $\mathrm{Re}_{\mathrm{c3}}$, the azimuthal angle of the IME increases monotonically towards $\pi/4$, with steeper rates for larger d/D.

As shown in Fig. 6, the values of $\mathrm{Re}_{\mathrm{c1}}$ and $\mathrm{Re}_{\mathrm{c3}}$ ($\sim\mathrm{Re}_{\mathrm{c2}}$) depend considerably on the size ratio d/D; an increase in d/D from 0.075 to 0.175 increases $\mathrm{Re}_{\mathrm{c1}}$, whereas it decreases $\mathrm{Re}_{\mathrm{c3}}$. Extrapolation of these values beyond $d/D = 0.175$ in Fig. 6 suggests that the values of $\mathrm{Re}_{\mathrm{c1}}$ and $\mathrm{Re}_{\mathrm{c3}}$ may become comparable at some larger d/D (>0.175). In such cases, the particle migration behavior may differ from that in the present study ($d/D \sim 0.1$). Indeed, regime 2 could possibly disappear at large d/D. Our preliminary measurements for larger particles ($d/D = 0.25$) seem to support this because we have not yet found regime 2 for $d/D = 0.25$. Further studies are necessary to confirm this.

D. Intermediate equilibrium positions

In macroscale tube experiments for a size ratio $d/D = 0.11$, Miura *et al.* [21] reported that the CCE was found to arise initially in the band formed along the channel face at Re ~ 250, followed by a progressive shift almost parallel to the sidewall up to the diagonal with increasing Re. At Re ~ 500, they reached the diagonal, and a further increase in Re shifted the equilibrium position in the outward direction along the diagonal. Although all these equilibrium positions were called the CCE in Miura *et al.* [21], in the present paper, we distinguished the equilibrium positions that had not yet reached the diagonal as IME from the CCE located on the diagonal. In fact, as pointed out in Fig. 3, these two equilibrium positions have different features; the CCE always exists on the diagonal but becomes stable at Re larger than a critical value, $\mathrm{Re}_{\mathrm{c2}}$, whereas the IME emerges on the pSS ring in a limited range of Re between $\mathrm{Re}_{\mathrm{c1}}$ and $\mathrm{Re}_{\mathrm{c3}}$. We do not yet know all the properties of the IME, such as whether there is a single equilibrium position or multiple stable equilibrium positions on the pSS ring in that Re range or whether the azimuthal angle of the IME at Re $= \mathrm{Re}_{\mathrm{c1}}$ is zero or a finite value. Examining these issues will require future studies.

One of the key findings of the present study is that the values of $\mathrm{Re}_{\mathrm{c1}}$ and $\mathrm{Re}_{\mathrm{c3}}$ ($\sim\mathrm{Re}_{\mathrm{c2}}$) depend considerably on the size ratio d/D. That is, the range of Re for regime 2 varies significantly, depending on d/D. For $d/D = 0.075$, the range is rather large ($180 < \mathrm{Re} < 600$), whereas for $d/D = 0.175$ the range is rather small ($290 < \mathrm{Re} < 350$). For smaller particles ($d/D < 0.075$), $\mathrm{Re}_{\mathrm{c1}}$ may decrease, down to the range of the ordinary microchannel flows (<100). This trend, and the long entry length for smaller d/D, may be related to the statement in previous studies that particle focusing occurs for $d/D \geqslant 0.07$ in microchannel flows [4]. In the other limit of large d/D (>0.175), regime 2 may vanish, as noted above. Furthermore, a recent numerical study [18], using the lattice Boltzmann method, reported that the stability of the CFE and CCE was reversed for larger particles; that is, the CFE was unstable, and the CCE was stable at Re $\leqslant 20$ for $d/D \geqslant 0.3$ and at Re $\leqslant 40$ for $d/D \geqslant 0.4$, and the two equilibrium positions are not stable at the same time. Because the CFE is always stable for $d/D \sim 0.1$, as treated in the present study, this is a completely different behavior of particle migration, depending on the size ratio. The dependence of the migration properties on the size ratio may be an important issue to explore in more detail.

IV. CONCLUSIONS

In the present study, we observed directly the cross-sectional distributions of neutrally buoyant spherical particles in square tube flows in the Re range from 1 to 800 for particle-to-tube-size ratios from 0.075 to 0.175. From the evolution of the particle distribution along the flow up to a distance of 1500 times the tube width, we classified the lateral migration of particles into four regimes. In the first regime of the lowest Re range, particles were focused on the CFE in the downstream cross section, in accord with previous studies for microchannel flows, whereas in the second and third regimes, additional particle focusing was observed at the IME and CCE, respectively. In the fourth regime, the Re value was between the second and third regimes; these three types of equilibrium positions existed simultaneously. The critical Re values were found to depend significantly on the size ratio in such a way that an increase in particle size may diminish the Re range of the second regime.

ACKNOWLEDGMENT

This research was partially supported by JSPS KAKENHI and the ORDIST group fund at Kansai University.

---

[1] G. Segre and A. Silberberg, Radial particle displacements in Poiseuille flow of suspensions, Nature (London) **189**, 209 (1961).

[2] G. Segre and A. Silberberg, Behaviour of macroscopic rigid spheres in Poiseuille flow: Part 2. Experimental results and interpretation, J. Fluid Mech. **14**, 136 (1962).

[3] F. P. Bretherton, The motion of rigid particles in a shear flow at low Reynolds number, J. Fluid Mech. **14**, 284 (1962).

[4] D. Di Carlo, D. Irimia, R. G. Tompkins, and M. Toner, Continuous inertial focusing, ordering, and separation of particles in microchannels, Proc. Natl. Acad. Sci. USA **104**, 18892 (2007).

[5] A. A. S. Bhagat, S. S. Kuntaegowdanahalli, and I. Papautsky, Enhanced particle filtration in straight microchannels using shear-modulated inertial migration, Phys. Fluids **20**, 101702 (2008).

[6] Y. W. Kim and J. Y. Yoo, The lateral migration of neutrally-buoyant spheres transported through square microchannels, J. Micromech. Microeng. **18**, 065015 (2008).

[7] D. Di Carlo, Inertial microfluidics, Lab Chip **9**, 3038 (2009).

[8] A. Karimi, S. Yazdi, and A. M. Ardekani, Hydrodynamic mechanisms of cell and particle trapping in microfluidics, Biomicrofluidics **7**, 021501 (2013).

[9] H. Amini, W. Lee, and D. Di Carlo, Inertial microfluidic physics, Lab Chip **14**, 2739 (2014).

[10] J. Zhang, S. Yan, D. Yuan, G. Alici, N. T. Nguyen, M. E. Warkiani, and W. Li, Fundamentals and applications of inertial microfluidics: A review, Lab Chip **16**, 10 (2016).

[11] D. Di Carlo, J. F. Edd, K. J. Humphry, H. A. Stone, and M. Toner, Particle Segregation and Dynamics in Confined Flows, Phys. Rev. Lett. **102**, 094503 (2009).

[12] Y. S. Choi, K. W. Seo, and S. J. Lee, Lateral and cross-lateral focusing of spherical particles in a square microchannel, Lab Chip **11**, 460 (2011).

[13] A. T. Ciftlik, M. Ettori, and M. A. M. Gijs, High throughput-per-footprint inertial focusing, Small **9**, 2764 (2013).

[14] A. A. S. Bhagat, S. S. Kuntaegowdanahalli, and I. Papautsky, Inertial microfluidics for continuous particle filtration and extraction, Microfluid. Nanofluid. **7**, 217 (2009).

[15] K. J. Humphry, P. M. Kulkarni, D. A. Weitz, J. F. Morris, and H. A. Stone, Axial and lateral particle ordering in finite Reynolds number channel flows, Phys. Fluids **22**, 081703 (2010).

[16] J. Zhou and I. Papautsky, Fundamentals of inertial focusing in microchannels, Lab Chip **13**, 1121 (2013).

[17] M. Abbas, P. Magaud, Y. Gao, and S. Geoffroy, Migration of finite sized particles in a laminar square channel flow from low to high Reynolds numbers, Phys. Fluids **26**, 123301 (2014).

[18] C. Prohm and H. Stark, Feedback control of inertial microfluidics using axial control forces, Lab Chip **14**, 2115 (2014).

[19] K. Hood, S. Lee, and M. Roper, Inertial migration of a rigid sphere in three-dimensional Poiseuille flow, J. Fluid Mech. **765**, 452 (2015).

[20] C. Liu, G. Hu, X. Jian, and J. Sun, Inertial focusing of spherical particles in rectangular microchannels over a wide range of Reynolds numbers, Lab Chip **15**, 1168 (2015).

[21] K. Miura, T. Itano, and M. Sugihara-Seki, Inertial migration of neutrally buoyant spheres in a pressure-driven flow through square channels, J. Fluid Mech. **749**, 320 (2014).

[22] B. Chun and A. J. C. Ladd, Inertial migration of neutrally buoyant particles in a square duct: An investigation of multiple equilibrium positions, Phys. Fluids **18**, 031704 (2006).

[23] N. Nakagawa, T. Yabu, R. Otomo, A. Kase, M. Makino, T. Itano, and M. Sugihara-Seki, Inertial migration of a spherical particle in laminar square channel flows from low to high Reynolds numbers, J. Fluid Mech. **779**, 776 (2015).

[24] Y. S. Choi and S. J. Lee, Holographic analysis of three-dimensional inertial migration of spherical particles in micro-scale pipe flow, Microfluid. Nanofluid. **9**, 819 (2010).

[25] H. Yamashita and M. Sugihara-Seki, Numerical simulation for the motion of a spherical particle in laminar square duct flows, Sci. Technol. Rep. of Kansai Univ. **59**, 39 (2017).

[26] T. Kajishima, S. Takiguchi, H. Hamasaki, and Y. Miyake, Turbulence structure of particle-laden flow in a vertical plane channel due to vortex shedding, JSME Int. J., Ser. B **44**, 526 (2001).

[27] See Supplemental Material at http://link.aps.org/supplemental/10.1103/PhysRevFluids.2.044201 for more information of the experimental method, experimental results, and numerical results.